Acta Astronautica 172 (2020) 140–150

Contents lists available at ScienceDirect

Acta Astronautica

journal homepage: www.elsevier.com/locate/actaastro

Research paper

Analysis of shock-wave diffraction over double cylindrical wedges. Part II: Vorticity generation

N. Brahmi[a,*], A. Hadjadj[a], V. Soni[a], A. Chaudhuri[b]

[a] Normandie University, INSA of Rouen, CNRS, CORIA, 76000, Rouen, France
[b] Department of Civil Engineering and Energy Technology, OsloMet – Oslo Metropolitan University, Pilestredet 35, PB 4, St. Olavs Plass, 0130, Oslo, Norway

ARTICLE INFO

Keywords:
Shock wave
Shock diffraction
Vorticity
Vorticity transport
Numerical simulation

ABSTRACT

The unsteady aspect of turbulent flow structures generated by a shock-wave diffraction over double cylindrical wedges, with initial diffracting angle of 75°, are numerically investigated by means of two-dimensional high-fidelity numerical simulation. Different incident-shock-Mach numbers, ranging from transonic to supersonic regimes, are considered. Unlike previous studies where only the total vorticity production is evaluated, the current paper offers more insights into the spatio-temporal behavior of the circulation by evaluating the evolution of the instantaneous vorticity equation balance. The results show, for the first time, that the diffusion of the vorticity due to the viscous effects is quite important compared to the baroclinic term for low Mach numbers regimes, while this trend is inverted for higher Mach numbers regimes. It is also found that the stretching of the vorticity due to the compressibility effects plays an important role in the vorticity production. In terms of pressure impulses, the effect of the first concave surface on the shock strength has been quantified at both earlier and final stages of the shock diffraction process. Unlike the overpressure, the static and the dynamic pressure impulses are shown to be significantly reduced at the end of the first concave surface.

1. Introduction

The unsteady evolution of vortex rings produced by a shock diffraction undergoing a sudden expansion area is one of the most fascinating phenomenon in high-speed flows. This process was observed many decades ago [1–3], with different levels of qualitative description [4] and numerical modelling [5–7]. For instance, Skews [1] have discussed the behavior of disturbances produced in the perturbed region caused by the passage of a shock wave, whose Mach number varies from 1.0 to 5.0, through a convex corner. The experimental results of this study have shown that the velocities of the contact surface and the secondary shock become independent of the corner angles greater than 75°. Sun and Takayama [5] have evaluated numerically the vorticity production in a shock-wave diffraction problem over convex corners, with angles varied from 5° to 180°. The authors proposed an analytical model to evaluate the total vorticity production generated by the slipstream. They found that the rate of vorticity production is always increasing with the corner angle and the shock strength. They also reported that the slipstream is at the origin of the total vorticity generation and it can be the more dominating factor in producing vorticity in compressible flows in comparison to baroclinic effects. In another study, Sun and Takayama [8] have investigated the formation of secondary shock waves behind the incident shock wave. Accordingly, the threshold shock-wave Mach number was found to be $M_s = 1.346$ for a gas with $\gamma = 1.4$, when neglecting viscous effects on the formation of this secondary shock waves.

Quinn and Kontis [9] have investigated a shock-wave diffraction around a 172° corner at $M_s = 1.46$ using both numerical simulations and experimental visualizations. Their numerical study showed that although the evolution of the shear layer was obtained for very fine mesh, some very fine flow structures were under predicted. Cai et al. [10] have investigated the effect of back-pressure on the shock train location and its structure in a straight isolator. It is shown that the structure of the shock train largely depends on the relative Mach number and is very sensitive to it. Concerning the average back-pressure, it has a great influence on the location of the shock train in the oscillating region, while its amplitude has a noticeable effect on the size of this oscillating region. Reeves and Skews [11] have investigated both numerically and experimentally the unsteady aspects of three-dimensional shock-wave diffraction phenomena. They found that the trends of circulation production correlated quite well with those obtained from the two-dimensional diffraction case. Furthermore, they showed that the rate of vorticity production tends to be constant once the incident shock wave had fully diffracted over the surface edge. Finally, the shape of the

* Corresponding author.
E-mail address: nassim.brahmi@insa-rouen.fr (N. Brahmi).

https://doi.org/10.1016/j.actaastro.2020.02.017
Received 28 January 2020; Received in revised form 7 February 2020; Accepted 9 February 2020
Available online 18 February 2020

Nomenclature

E	total energy per unit mass
e	internal energy per unit mass
I_p	static-pressure impulse
I_{pd}	dynamic-pressure impulse
M_s	incident-shock-Mach number
$\mathscr{P}$	normalized overpressure
Pr	Prandtl number
p	static pressure
$\mathscr{R}$	universal gas constant
R	concave radius
T	temperature
t	time
$\mathbf{v}$	velocity vector

Greeks

Γ	vorticity circulation
γ	heat capacity ratio
λ	thermal conductivity
μ	dynamic viscosity
ρ	density
ω	local vorticity
ω_1	angle of the first wedge
ω_2	angle of the second wedge
ω_c	convection vorticity term
ω_t	unsteady vorticity term

Abbreviations

BAR	baroclinic torque
DFV	diffusion of vorticity due to viscosity
IBM	immersed-boundary method
I	incident shock wave
LS	lambda shock
PV	primary vortex
r	reflected shock wave
SLI	shear-layer instabilities
SS	secondary shocks
SV	secondary vortex
VSC	stretching of vorticity due to compressibility
VSG	stretching/tilting of vorticity due to velocity gradients
VTE	vorticity transport equation
WENO	weighted essentially non-oscillatory

diffracting edge appeared to have no significant impact on the results.

Abate and Shyy [12] studied the dynamics of shock-wave diffraction using the vorticity transport equation. They discussed the link between high-strain rates resulting from the expansion corner to the solenoidal dissipation rates and the stress rates to the dilatational dissipation rates of turbulent kinetic energies. The baroclinic torque enhances the vorticity generation in such interaction. Their study indicates that both viscous effects and small-scale turbulent dissipation are important for the evolution of the primary vortex as well as the small vortices generated by the Kelvin-Helmholtz instability. Zhao et al. [13] have investigated the shock wave focusing process with shock-turbulence interaction in a parabolic cavity with various intensity of shock and vortex strength. Their numerical results show that the net dilatational vorticity is the most dominant part in vorticity transport, followed by the baroclinic vorticity and the viscous vorticity generation.

Gnani et al. [4] have used experimental schlieren photography to qualitatively evaluate the development of a shock-wave diffraction around sharp and curved splitters. Recently, Chaudhuri and Jacobs [7] performed numerical analysis of shock-wave diffraction over a sharp splitter plate. The objective was to address a detailed analysis of the flow evolution using the probability density functions of various enstrophy equation parameters as well as the invariants of the velocity gradient tensor. Their study reveals the mechanism of unwinding of vortices and its link with the divergence of the Lamb vector.

Additionally, Tseng and Yang [6] investigated numerically shock-wave diffraction around a convex corner by solving both Euler and Navier-Stokes equations. The vorticity production formed during the shock-wave diffraction and the subsequent interaction between the reflected shock and the main vortex core have been analyzed. Different circulation production rates are observed between Euler and Navier-Stokes solutions as a result of the vorticity contribution from the boundary layer and the secondary vortex. It was also found that the reflection influences the rate of vorticity production, which is found to be dependent on the strength of the incident shock wave and the diffracting angle.

Chaudhuri et al. [14] used an immersed boundary (IB) method to study the interaction of the moving shock through an array of cylinder matrix. Their analysis confirmed earlier findings of Sun and Takayama [5], where the baroclinic production of the vorticity is found to be feeble. Recently, Soni et al. [15] have conducted numerical investigations of shock-wave reflection over double-concave cylindrical reflectors, where new shock reflection topologies were found.

The aim of the present study is to further analyze the evolution of the instantaneous vorticity production and the flow structure in shock diffraction problem.

2. Governing equations and numerics

The compressible Navier-Stokes equations for an ideal gas are given by:

$$\partial_t \rho + div(\rho\, \mathbf{v}) = 0 \tag{1}$$

$$\partial_t (\rho\, \mathbf{v}) + div(\rho\, \mathbf{v} \otimes \mathbf{v}) + \nabla p = \nabla \tau \tag{2}$$

$$\partial_t (\rho\, E) + div(\rho\, E\, \mathbf{v}) + div(\rho\, \mathbf{v}) = \nabla(\tau\, \mathbf{v} + \lambda \nabla T) \tag{3}$$

$$p = (\gamma - 1)\rho\, e, \qquad E = \frac{1}{2}\left|\mathbf{v}\right|^2 + e \tag{4}$$

$$\tau = \mu\left[\nabla \otimes \mathbf{v} + (\nabla \otimes \mathbf{v})^T - \frac{2}{3}(\nabla \cdot \mathbf{v})\mathbf{I}\right] \tag{5}$$

where t stands for the time, ρ, $\mathbf{v}$, p, E, T, λ, μ, e are the density, velocity vector, pressure, total energy per unit mass, temperature, thermal conductivity, dynamic viscosity and internal energy, respectively. The working gas is air with $\gamma = 1.4$ and Prandtl number $Pr = 0.72$. The fluid viscosity follows Sutherland's law.

To simulate the flow field, we used an *in-house* compressible parallel solver equipped with adaptive multi-resolution method [16,17] for mesh refinement. The code uses an immersed-boundary method (IBM)

Table 1
Different grid resolutions used for a given incident shock-wave Mach number of $M_s = 1.6$ (MP: million points).

Grid	$\Delta x_{min}(\mu m)$	$\Delta y_{min}(\mu m)$	number of points (MP)
$\mathscr{G}_0$	95	88	1.83
$\mathscr{G}_1$	60	50	5.04
$\mathscr{G}_2$	40	40	8.84
$\mathscr{G}_3$	30	29	17.3
$\mathscr{G}_4$	20	21	33.55

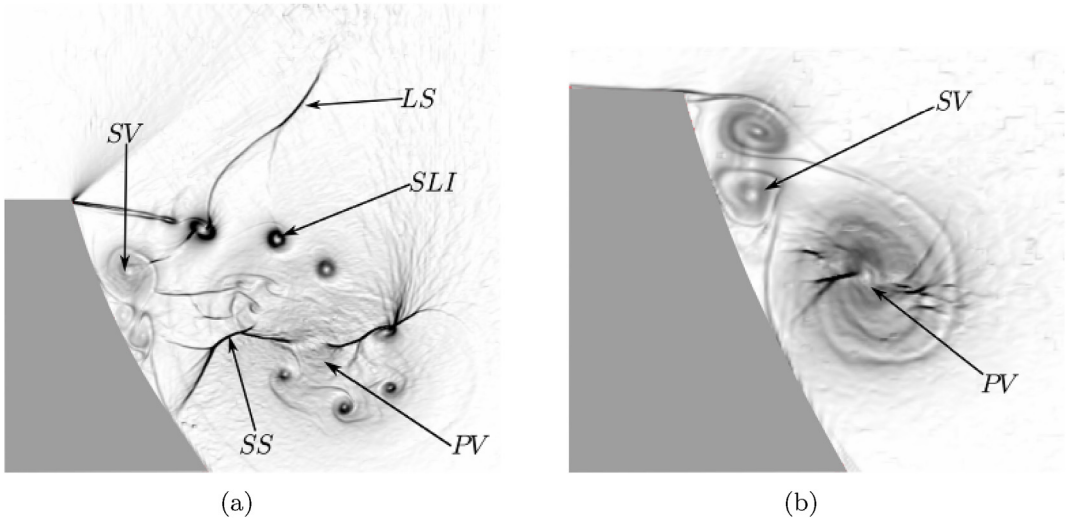

Fig. 1. Numerical schlieren pictures for $M_s = 1.6$ (a): first concave at $t = 184\ \mu s$ (b): second concave at $t = 292\ \mu s$. PV: Primary vortex, SV: Secondary vortex, LS: Lambda shock, SLI: Shear layer instabilities, SS: secondary shock (shocklets).

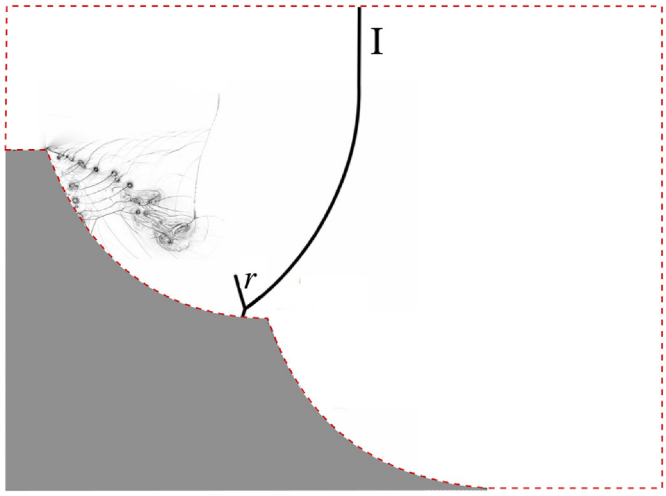

Fig. 2. Schematic representation of double concave surfaces, – – – integral path L, I: incident shock wave, *r*: reflected shock wave.

to handle fluid-solid interaction problems [14,18]. The solid body is embedded into a Cartesian grid and tracked using a ray-tracing technique. Inviscid and viscous fluxes are computed using a fifth-order weighted essentially non-oscillatory (WENO 5) scheme and a fourth-order central difference formula, respectively, while the time is advanced using a third-order Runge-Kutta method [19].

3. Problem set-up

As in Brahmi et al. [20], a two-dimensional problem of shock diffraction over double concave geometry, with constant radius of $R = 50$ *mm* and wedge angles $\omega_1 = \omega_2 = 75°$, is considered. As for the computational specifications, the boundary conditions were set to inlet and outlet at the left and the right sides of the computational domain, respectively, while the top and the bottom-right boundaries are considered as symmetry planes. On the solid surface, no-slip boundary conditions are applied. The incident-shock-Mach number was varied from 1.6 to 4.5. For all those Mach numbers, the shock is initially located 5 *mm* ahead of the first concave surface corner. Rankine-Hugoniot relations are used to fix the initial conditions for both left (shocked gas) and right (stagnant flow) states at a given M_s. Air is considered as a working fluid and the initial stagnant flow is assigned with temperature $T_0 = 300\ K$ and pressure $p_0 = 101.3\ kPa$. Given the sensitivity of the phenomena to the grid resolution, a grid dependency study is conducted in order to determine the grid resolution effect on the results. Five different meshes were used for $M_s = 1.6$, as summarized in Table 1.

4. Results and discussion

Fig. 1(a) and (b) show the flow structures behind the diffracting shock wave for the first and the second concave surfaces, respectively. Shortly after the penetration of the shock into the cavity, the expanding flow evolves into a complicated system of distorted and secondary shocks with separated regions and vortices formation. As shown in Fig. 1, an end-wall corner vortex (PV) is formed at $M_s = 1.6$ with a rolling-up of eddies that are convected away from the concave entrance as the diffraction process evolves. In addition to this important primary vortex, a secondary instability (SV) appears along the surface wall. The Reynolds number, based on the shocked flow properties (density, speed of sound, viscosity in the upstream of the shock and the radius of curvature *R*), is of the order of 10^6.

4.1. Vorticity production

In order to investigate the dynamics of the shear-layer formation, the vorticity production is first analyzed in term of total circulation Γ as:

$$\Gamma = \int_s \omega\, ds = \int_L u\, dl \tag{6}$$

where the integral contour (path L) is taken along the boundary so that to enclose the perturbed region behind the shock wave. The integral contour is depicted in Fig. 2 by a dashed red line. For better characterization of the vorticity production in shock-wave diffraction, the ratio of circulation to time, Γ/t, is used. The rate of circulation production is related to the incident shock-Mach number M_s, the diffraction angle and the gas properties. For a given gas and diffraction angle, the ratio Γ/t can be uniquely determined as a function of M_s [5] as:

$$\frac{\Gamma}{t} = f(M_s) \tag{7}$$

In this paper, the calculation of the circulation is directly obtained from the summation of the vorticity over each individual surface area. In general, the calculation of the circulation is performed only in the perturbed region behind the shock. However, in this study the total amount of circulation is calculated over the entire computational

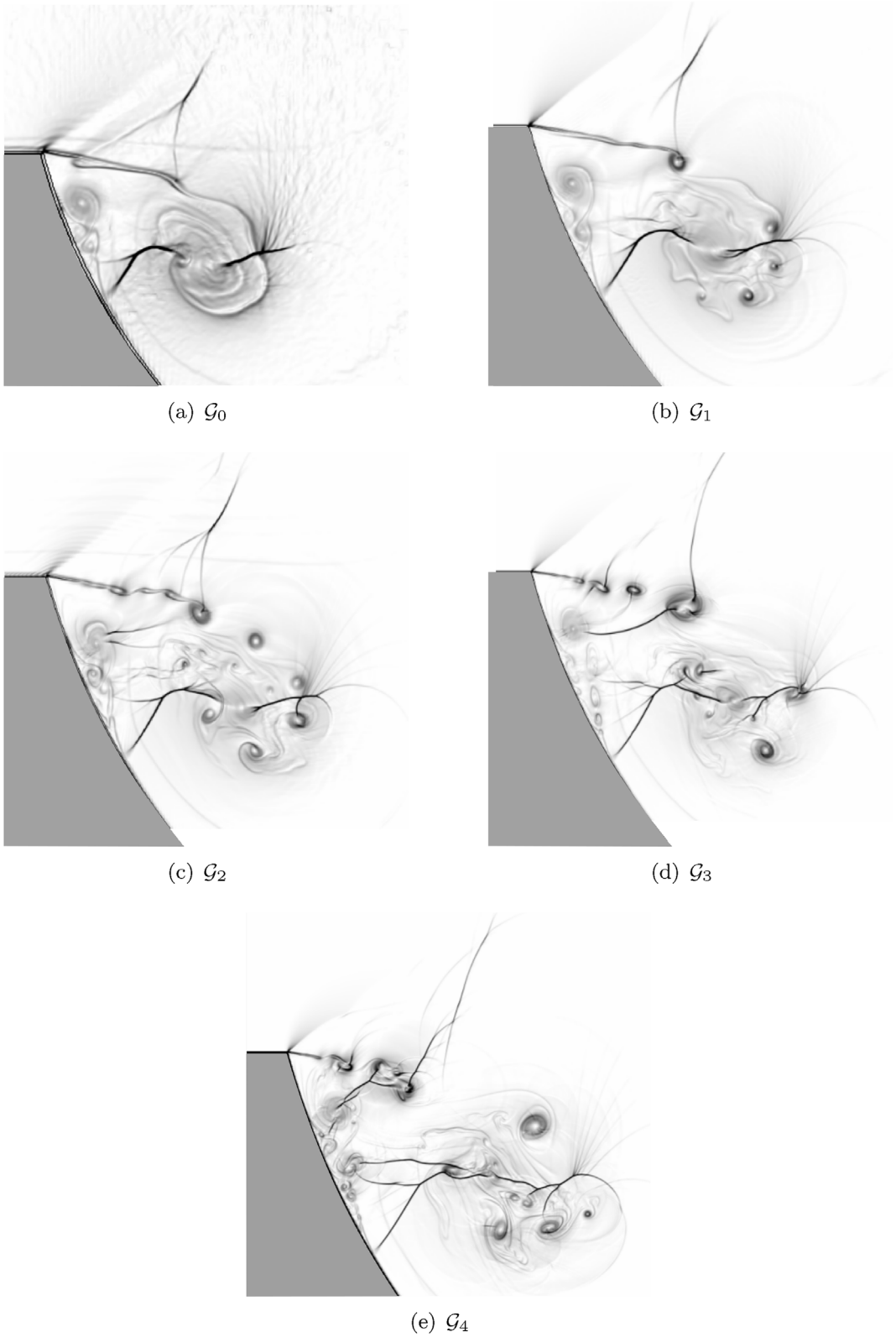

Fig. 3. Numerical schlieren pictures for different grid resolutions at $t = 150\,\mu s$ with $M_s = 1.6$.

domain since the unperturbed flow regions (uniform flow) provides almost no contribution to the circulation.

As it can be seen in Fig. 3, the flow topology of the primary vortex changes with the mesh resolution, the global variation of the vorticity production (Γ) and its rate (Γ/t) are insensitive to the grid resolution (see Fig. 4(a) and (b)). Indeed, the circulation Γ increases linearly in time regardless of the grid resolution. The results for the rate of vorticity production (Γ/t) are scaled by the product $\mathscr{R} \times T_0$, where $\mathscr{R}$ is the universal gas constant divided by the molecular weight of air taken as, $\mathscr{R} = 287\ J.\ Kg^{-1}.\ K^{-1}$ and T_0 is the temperature in front of the incident shock ($T_0 = 300\ K$). Since the rate has the dimension of the square of the velocity ($m^2 s^{-2}$), one may obtain dimensional results by multiplying the

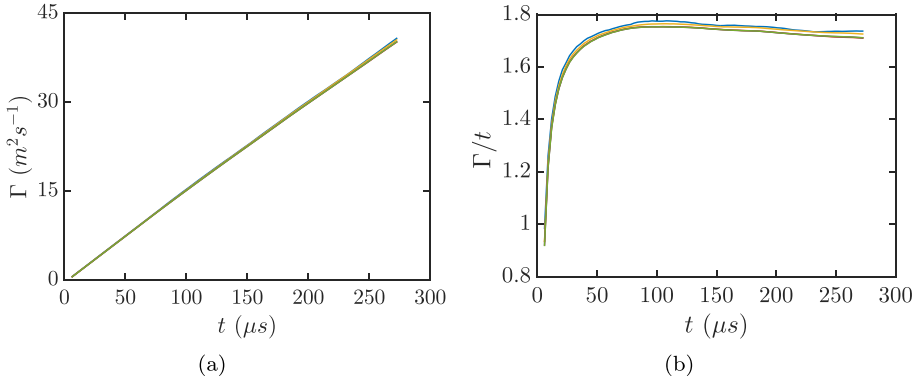

Fig. 4. Time history of (a): circulation (b): rate of circulation production for $M_s = 1.6$ and different mesh resolutions (– $\mathscr{G}_0$, – $\mathscr{G}_1$, – $\mathscr{G}_2$, – $\mathscr{G}_3$, – $\mathscr{G}_4$).

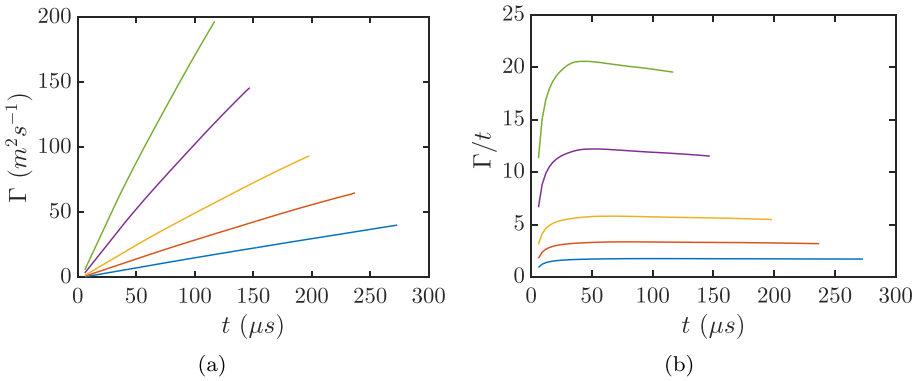

Fig. 5. Time history of (a): circulation (b): rate of circulation production for different incident-shock-Mach numbers (– $M_s = 1.6$, – $M_s = 2.0$, – $M_s = 2.5$, – $M_s = 3.5$, – $M_s = 4.5$).

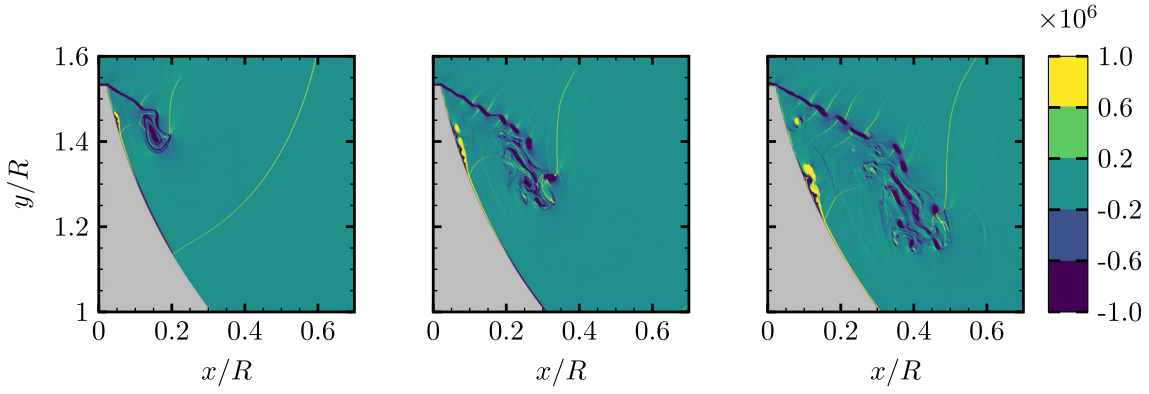

Fig. 6. Vorticity maps for $M_s = 2.0$. Column-wise (left-to-right): $t = 48\,\mu s$, $78\,\mu s$ and $108\,\mu s$.

dimensionless values by $\mathscr{R} \times T_0$,

$$\frac{\Gamma'}{t'} = \mathscr{R} \times T_0 \frac{\Gamma}{t} \tag{8}$$

Note that all the results of the rate of vorticity production, Γ/t, presented in this paper are dimensionless values.

The effect of shock strength on the vorticity production is investigated by changing M_s using the grid $\mathscr{G}_4$. The results are shown in Fig. 5(a) and (b). Basically both quantities increase with M_s. In other words, the strength of the main vortex increases at higher values of Mach number, and increases much faster for stronger shock waves as reported by Sun and Takayama [5]. The vorticity production occurs before the diffraction of the incident shock wave (at $t = 12\ \mu s$ for $M_s = 2.0$) as a result of the boundary-layer formation on the solid wall. This demonstrates the role played by viscous effects in forming the shock-wave diffraction structure as mentioned by Tseng and Yang [6].

Fig. 5(b) shows the rate of the circulation production. The five curves reach different constant values of 1.78, 3.79, 5.72, 11.42 and 18.73 for $M_s = 1.6$, 2.0, 2.5, 3.5 and 4.5, respectively. Similar trends were observed by Sun and Takayama [5] with constant values known as invariants of Euler equations in shock-wave diffraction.

Fig. 6 represents vorticity maps at different instants ($t = 48\,\mu s$, $78\,\mu s$ and $108\,\mu s$) for $M_s = 2.0$. As it can be seen, the main vortex and the highly disturbed shear layer split when interacting with the secondary shock waves. This results in a generation of fine scale turbulent eddies. Note that the production of vorticity is mainly concentrated in this turbulent region compared to the compression zone.

4.2. Vorticity transport equation

The vorticity transport equation provides further details on the mechanism of the vortex dynamics, it can be written as follows:

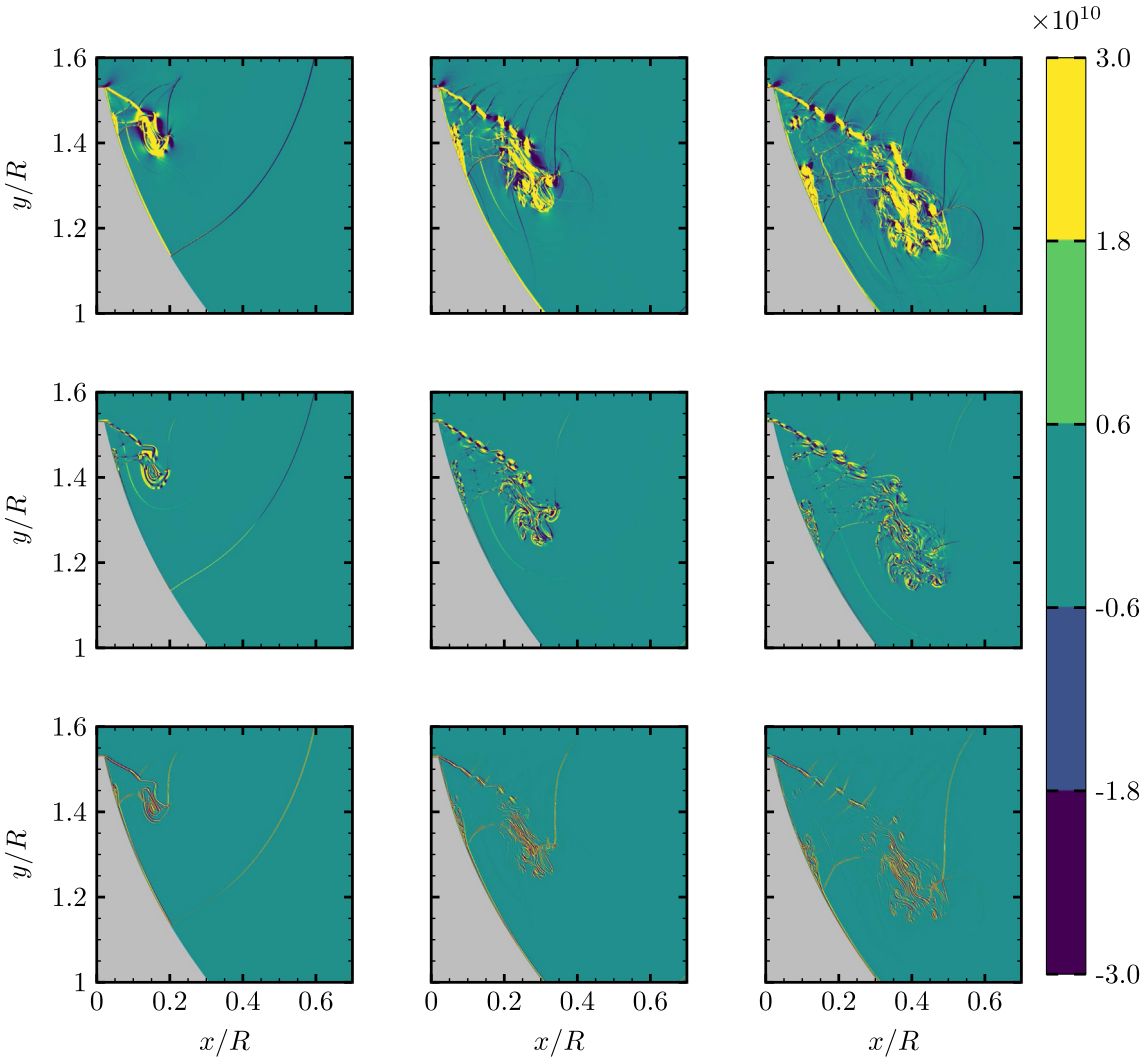

Fig. 7. Color maps of vorticity terms for $M_s = 2.0$. Row-wise (top-to-bottom): stretching of the vorticity due to flow compressibility (VSC), baroclinic (BAR) and diffusion of vorticity due to the viscous effects (DFV) terms. Column-wise (left-to-right): $t = 48\,\mu s$, $78\,\mu s$ and $108\,\mu s$.

$$\frac{D\omega}{Dt} = \underbrace{(\omega\cdot\nabla)u}_{\text{VSG}} - \underbrace{\omega(\nabla\cdot u)}_{\text{VSC}} + \underbrace{\frac{1}{\rho^2}(\nabla\rho\times\nabla p)}_{\text{BAR}} + \underbrace{\nabla\times\left(\frac{\nabla\cdot\tau}{\rho}\right)}_{\text{DFV}} \tag{9}$$

where the left-hand side represents the material derivative expressed as the sum of unsteady, ω_t, and convection, ω_c, terms. Here, $\omega_t = \partial\omega/\partial t$ and $\omega_c = U(\partial\omega/\partial x) + V(\partial\omega/\partial y)$.

The first term in the right-hand side of Eq. (9) represents the stretching or tilting of vorticity due to the flow velocity gradients, a term that is null in two-dimensional cases. The second term expresses the stretching of vorticity due to flow compressibility. The third contribution represents the baroclinic term, which accounts for the changes in the vorticity due to the intersection of density and pressure surfaces. The last term represents the diffusion of vorticity due to the viscous effects.

The different expressions appearing in the right-hand side of Eq. (9) are shown in Fig. 7 (in Row-wise) at different time intervals for $M_s = 2.0$. As one can see, the stretching of the vorticity due to flow compressibility (VSC) has the most dominant contribution. Based on the VSC contour, it is clear that there exist locally stretched structures in the core region of the vortex due to compressibility effect arising from local regions of compression/expansion. Additionally the results show the existence of evolving large scale vortices which interact with the different shock patterns present in the flow and finally split into small-scale vortices.

Fig. 8 shows the temporal evolution of the vorticity transport equation (VTE) terms. The stretching of vorticity due to flow compressibility (VSC) is almost constant over time independently of M_s, while its magnitude increases with Mach number. This contribution represents the effects of expansion on the vorticity field and plays a major role in the vorticity dynamics. The baroclinic term (BAR) is responsible of the generation of vorticity from unequal acceleration as a result of nonaligned density and pressure gradients. The lighter density fluid is faster accelerated than the high density one, which result in a shear-layer formation, that contributes to the generation of vorticity. The diffusion of vorticity due to the viscous effects (DFV) is essentially enhancing the viscous diffusion process on the vorticity distribution. As a result of viscosity, the vorticity tends to spread out spatially. Note that the diffusion of vorticity due to viscous effects (DFV) is quite important compared to the baroclinic term (BAR) for $M_s \leq 2.5$, while this trends is inverted for $Ms \geq 3.5$. As for the VSC term, the unsteady term, ω_t, which describes the rate of change in vorticity due to flow unsteadiness, is found to be constant in time regardless of M_s. For the convection term, ω_c, we also notice that it is almost constant in time for all shock-wave Mach numbers, and its magnitude increases at higher values of M_s. This term represents the change of vorticity of the moving fluid particles due to the motion of the fluid particle as it moves from one point to another.

Fig. 9 represents contours plots of ω_c for $M_s = 2.0$ at different

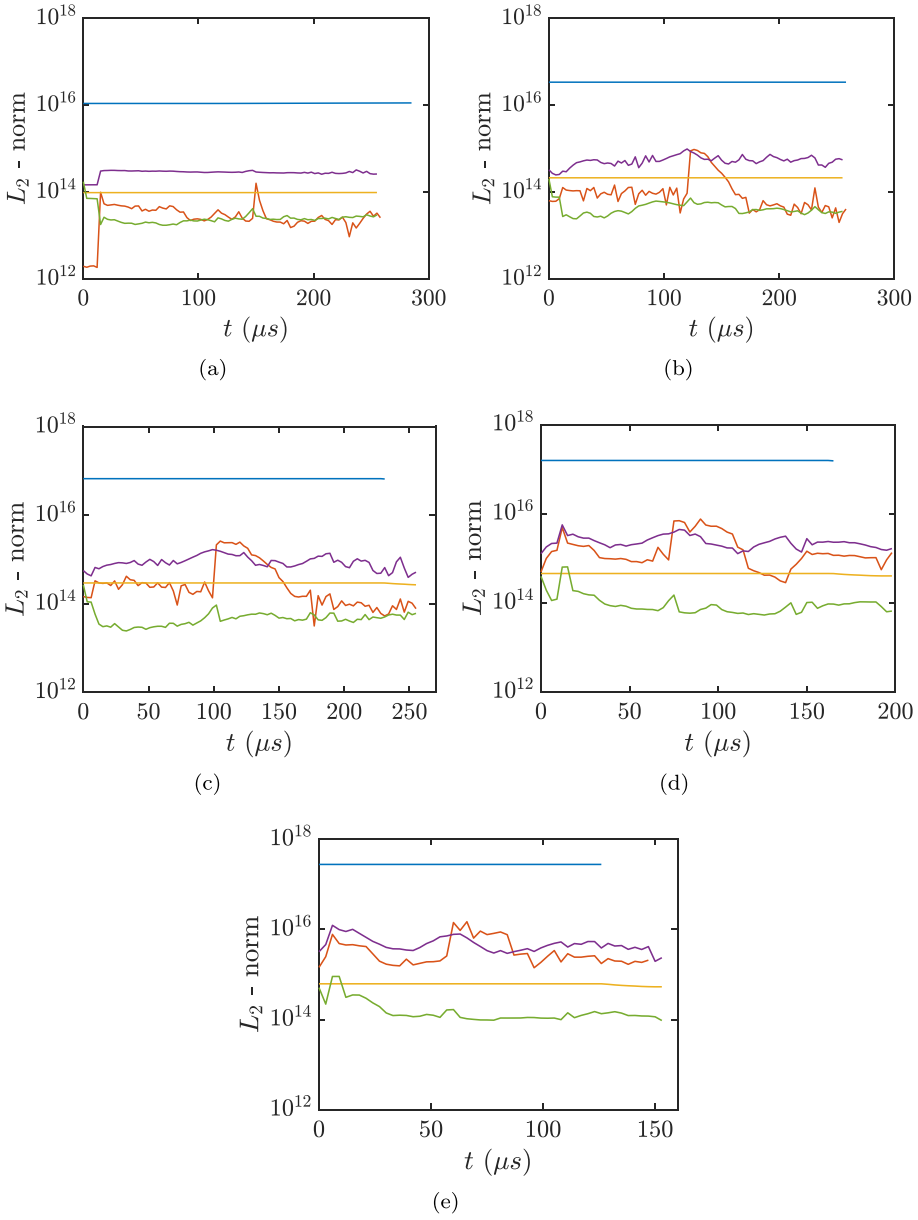

Fig. 8. Time history of normalized vorticity transport equation terms for (a): $M_s = 1.6$; (b): $M_s = 2.0$; (c): $M_s = 2.5$; (d): $M_s = 3.5$ and (e): $M_s = 4.5$ (¯: stretching of the vorticity due to flow compressibility (VSC) term, ¯: baroclinic (BAR) term, ¯: diffusion of vorticity due to the viscous effects (DFV) term, ¯: convection term (ω_c), ¯: unsteady term (ω_t)).

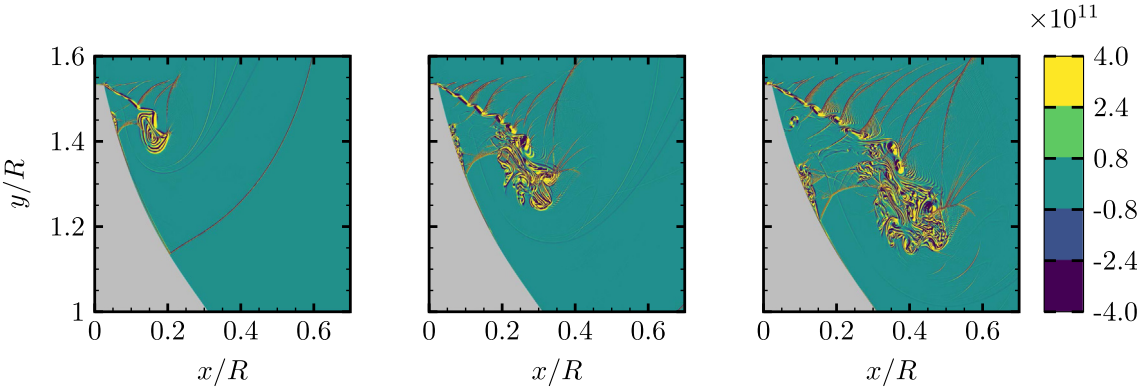

Fig. 9. Color maps showing the convection term of vorticity (ω_c) for $M_s = 2.0$. Column-wise (left-to-right): $t = 48\ \mu s$, $78\ \mu s$ and $108\ \mu s$.

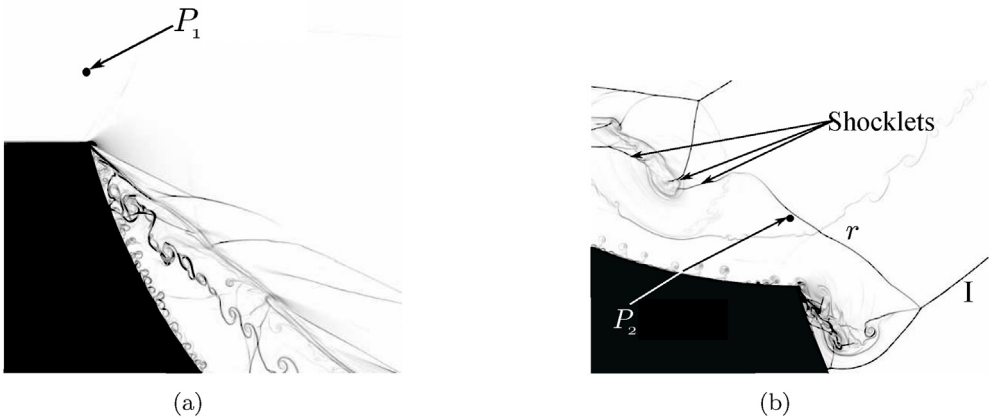

Fig. 10. Numerical schlieren pictures for $M_s = 4.5$ at $t = 69\ \mu s$: (a) beginning of the first concave surface; (b) beginning of the second concave surface; I: incident shock wave; r: reflected shock wave, P_1 and P_2 are two probes locations.

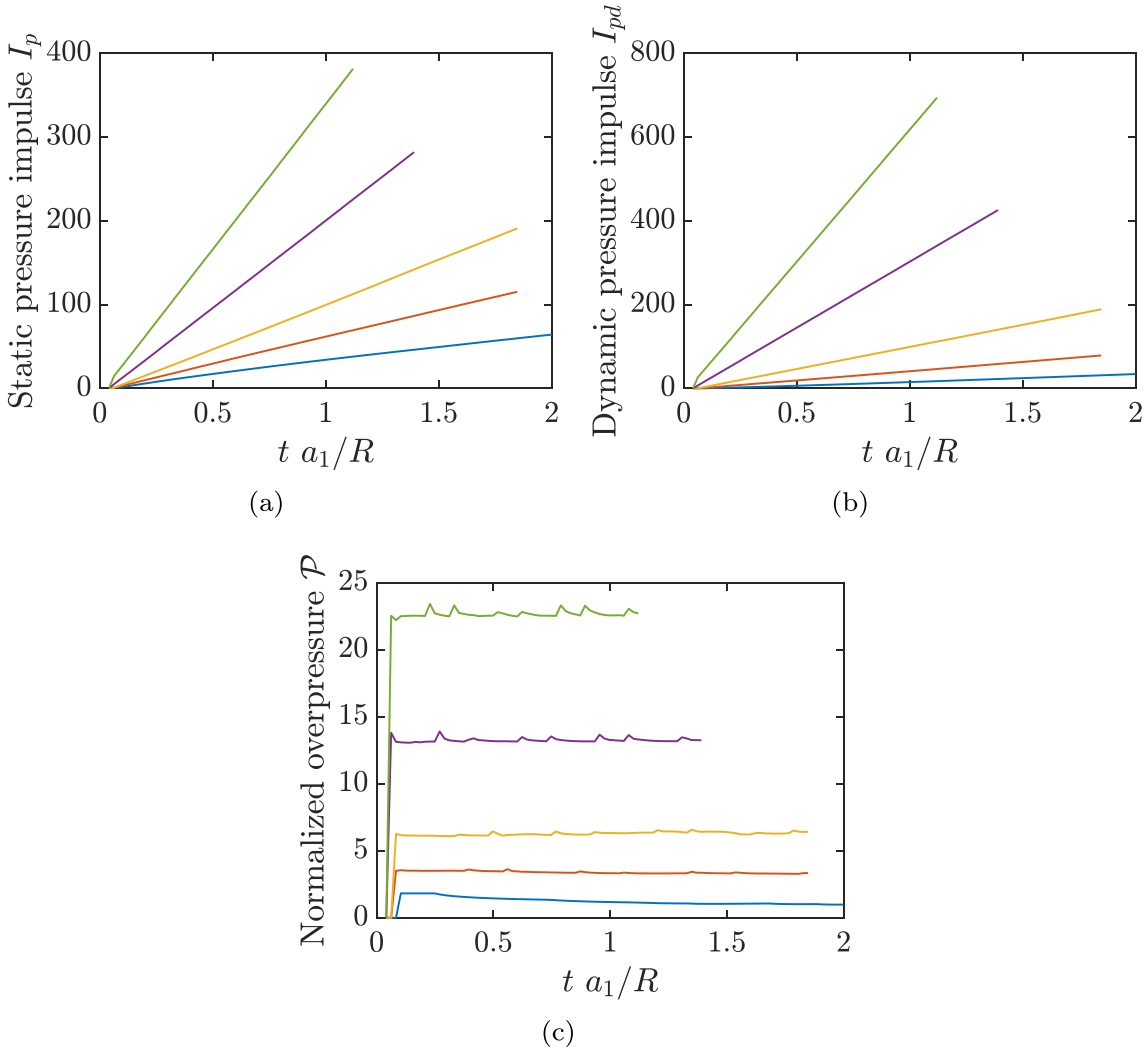

Fig. 11. Time history of (a): static pressure impulse, I_P (b): dynamic pressure impulse, I_{Pd} and (c): normalized overpressure $\mathcal{P}$, for different M_s at P_1 (– $M_s = 1.6$, – $M_s = 2.0$, – $M_s = 2.5$, – $M_s = 3.5$, – $M_s = 4.5$).

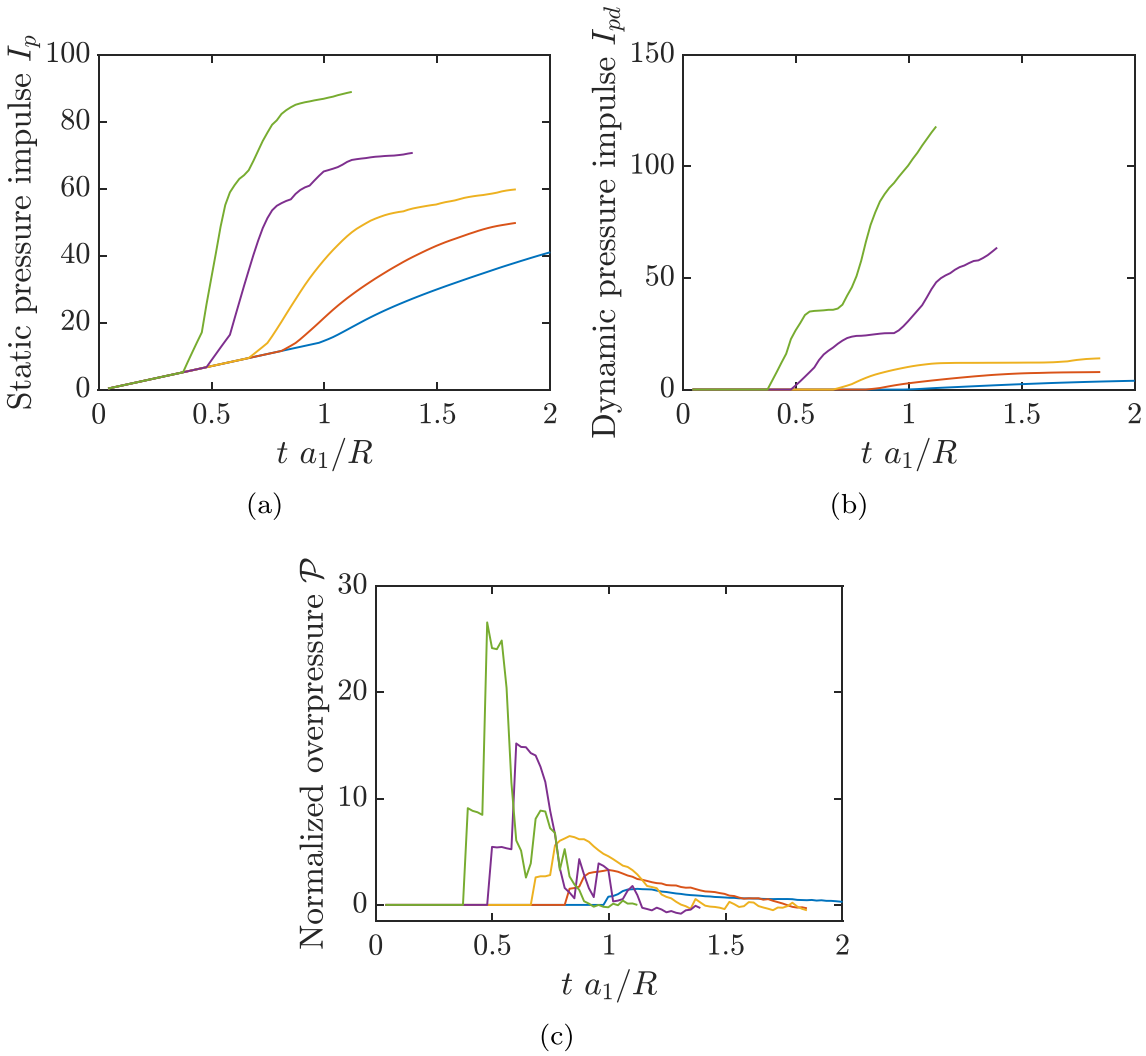

Fig. 12. Time history of (a): static pressure impulse, I_P (b): dynamic pressure impulse, I_{Pd} and (c): normalized overpressure $\mathscr{P}$, for different M_s at P_2 (– $M_s = 1.6$, – $M_s = 2.0$, – $M_s = 2.5$, – $M_s = 3.5$, – $M_s = 4.5$).

instants. As we can see, this term is mainly concentrated in the turbulent region as well as in the shear layer and in the near wall-region.

4.3. Static and dynamic pressure impulses and normalized overpressure

The effect of M_s on shock strength was investigated by computing the static and the dynamic pressure impulses along with the normalized overpressure, all defined as:

$$I_p = \int_{t_0}^{t_f} p\ dt \tag{10}$$

$$I_{pd} = \int_{t_0}^{t_f} \frac{1}{2}\rho\ \mathbf{v}^2\ dt \tag{11}$$

$$\mathscr{P} = (p - p_0)/p_0 \tag{12}$$

where p_0 is the static pressure of gas at rest, p, ρ and $\mathbf{v}$ are the local static pressure, density and velocity vector in the shocked region (t_0 and t_f being the initial and the final times). These quantities are calculated at two different space locations as shown in Fig. 10, with $P_1(x_1^*, y_1^*)$ corresponding to the beginning of the first concave surface, $x_1^* = x_1/R = 0.26$ and $y_1^* = y_1/R = 1.6$ and $P_2(x_2^*, y_2^*)$ corresponding to the beginning of the second concave surface, $x_2^* = x_2/R = 1.22$ and $y_2^* = y_2/R = 0.86$. The results are presented in Figs. 11 and 12, for P_1 and P_2, respectively.

At the upstream location, P_1, both static and dynamic pressure impulses are linearly increasing with time for all M_s. The passage of the incident wave is characterized by a sudden jump in these last two quantities (more visible for $M_s = 4.5$ as seen in Fig. 11(a) and (b)). This linear increase is due to the fact that P_1 is located at the inlet where no perturbation exists behind the shock wave. Concerning the normalized overpressure, one can see in Fig. 11(c) a sudden jump caused by the passage of the incident shock. Afterwards, it remains constant, except for $M_s = 1.6$, where it starts to decrease gradually as the shock propagates over the double concave surfaces.

At the downstream location, P_2, the flow behavior is completely different. The static pressure impulse is suddenly increased due to the passage of the shock. At this early stage of the diffraction process, the increasing rate is important. However, after the shock wave leads off the end of the geometry, it decreases giving almost constant value (see Fig. 12(a)). For the dynamic pressure impulse, we observe a sudden increase induced by the passage of the shock, after this it remains constant for a certain elapsed time until the arrival of the reflected shock and formation of the shocklets which generate a second increase due to the gas acceleration. Note that this behavior is more visible for $M_s = 4.5$ and $M_s = 3.5$ (see Fig. 12(b)). The arrival of the incident shock wave causes a sudden increase of the normalized overpressure (Fig. 12(c)). Afterwards, it remains almost constant until the reflected wave (r in Fig. 10(b)) arrives and causes a second increase. Once the reflected shock passed, the expanded gas gets driven away and causes a

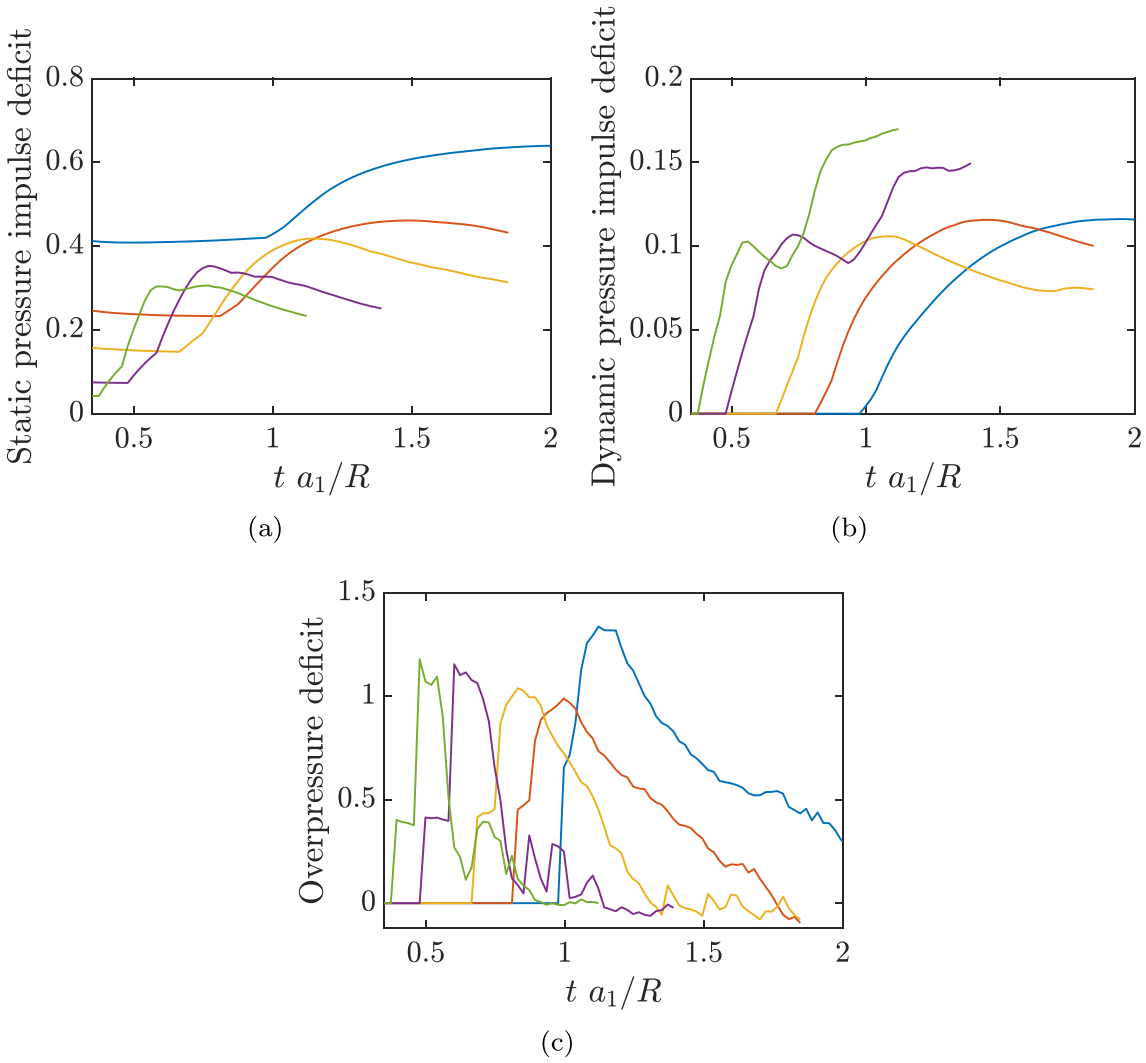

Fig. 13. Time history of (a): static pressure impulse deficit (b): dynamic pressure impulse deficit and (c): overpressure deficit, for different M_s at P_2 (– $M_s = 1.6$, – $M_s = 2.0$, – $M_s = 2.5$, – $M_s = 3.5$, – $M_s = 4.5$).

Table 2
Error estimates.

Allowable error (%)	Grid resolution	Physical time simulated (μs)	Number of time steps	Accumulated error	Allowable number of time steps	Reliability $R_s = \eta_{max}/\eta$
5	1793 × 1025	294	4311	9.48×10^{-16}	2.78×10^{27}	6.45×10^{23}
5	2817 × 1793	294	7854	5.84×10^{-17}	7.33×10^{29}	9.33×10^{25}
5	3841 × 2305	294	10307	1.8×10^{-17}	7.71×10^{30}	7.48×10^{26}
5	5633 × 3073	294	14061	6.94×10^{-18}	5.19×10^{31}	3.69×10^{27}
5	7681 × 3585	294	18728	7.14×10^{-19}	4.87×10^{33}	2.61×10^{29}

strong decrease. At the last stage of the diffraction, we can see a succession of peaks due to the passage of the shocklets and the emergence of flow instabilities in this zone. These peaks are visible only for high Mach numbers ($M_s = 4.5$, $M_s = 3.5$), for which the turbulent region is highly perturbed. It is worth noticing that for high M_s the flow relaxes until it reaches negative overpressure values, because of the strong vortex suction acting on this highly perturbed turbulent zone.

In order to investigate the effect of the first concave surface on the shock strength, the deficit of various parameters mentioned above is calculated. This deficit is defined as the ratio of the impulses and overpressure calculated at the two points: $I_p(P_2)/I_p(P_1)$, $I_{pd}(P_2)/I_{pd}(P_1)$, $\mathscr{P}(P_2)/\mathscr{P}(P_1)$. For static pressure impulse, we can see that the deficit is more important for the high Mach numbers because of the highly turbulent region generated behind the strong shock wave and the intense vortex suction exerted on the flow (see Fig. 13(a)). By comparing the static and dynamic pressure impulses deficit (Fig. 13(a) and (b), respectively) we can see that the deficit in dynamic pressure impulse is more important because of the decrease of density and the square of velocity together. For the overpressure deficit (Fig. 13(c)), the peaks are exceeding unit, which means that the overpressure in P_2 is greater than in P_1 and this is mainly caused by the passage of the reflected shock which induces the formation of shocklets (small shocks embedded into turbulent region).

5. Accumulation of numerical errors

Estimating accuracy and errors accumulation is necessary in CFD, especially when dealing with high-fidelity numerical simulations.

Depending on the spatial resolution and on the numerical scheme, a definite error occurs due to numerical integration at each time step [21]. According to Smirnov et al. [21], the relative integration error for one-dimensional problem is:

$$S_1 = \left(\frac{h}{L_1}\right)^{k+1} \tag{13}$$

where h is the cell size, L_1 is the domain length and k the order of accuracy of the numerical scheme. For multi-dimensional problem, the integration errors can be summed up as:

$$S_{err} = \sum_{i=1}^{3} S_i \tag{14}$$

The maximal allowable number of time steps for solving a given problem could be determined by the following formula:

$$\eta_{max} = (S^{max}/S_{err})^2 \tag{15}$$

where S^{max} is the allowable value of the total error, which is presumed to be between 1% and 5%. Smirnov et al. [21] have introduced another important measurement of numerical errors suitable for high-performance computing, which is the ratio of the maximal allowable number of time steps η_{max} to the actual number of time steps used to obtain the results η:

$$R_s = \eta_{max}/\eta \tag{16}$$

According to Smirnov et al. [21], the parameter R_s can characterize the reliability of the numerical results, i.e. how far below the limit, the simulations were finalized. Indirectly, this parameter characterizes the accumulated error. The higher is the value of R_s, the lower is the error. On tending R_s to unity, the error tends to a maximal allowable value.

Table 2 summarizes the results of different grid resolutions and physical time in our simulations. As it can be seen, a quite high level of reliability is achieved in our case.

6. Conclusions

In this paper, shock-wave diffraction over double cylindrical wedges have been numerically investigated by means of two-dimensional high-fidelity numerical simulation. The objective was to study the flow structure and the vorticity formation with regards to the incident-shock-wave Mach number. Different grid resolutions were used in order to investigate the mesh sensitivity of the results. It was found that although the upstream flow topology (shape of the eddies) changes with the grid resolution, the vorticity production and the shock diffraction process are quite independent from the grid resolution. In terms of rate of vorticity production and circulation, it is shown that the shock strength enhances the vorticity production and the rate of vorticity production increases as the incident shock strength increases and remains virtually constant after an elapsed time. For the vorticity transport equation, it was found that the stretching of vorticity due to flow compressibility plays an important role in the vorticity dynamics, for low-Mach numbers regimes ($Ms \leq 2.5$). The diffusion of the vorticity due to the viscous effects is seen to be quite important compared to the baroclinic term, while this trends is inverted for higher Mach numbers regimes ($Ms \geq 3.5$). In terms of shock strength, it was found that the effect of the first concave surface is effective in decreasing sufficiently the dynamic pressure impulse (up to 90% for $M_s = 2.5$) as well as the static pressure impulse (up to 75% for $M_s = 4.5$). However for the overpressure deficit, the peaks are accentuated by the passage of the reflected shock and the formation of shocklets that tend to reduce the overall overpressure deficit.

Acknowledgments

The first author gratefully acknowledges support from the Algerian Government through a Ph.D Fellowship. Computational facilities from 'Centre Régional Informatique et d'Applications Numériques de Normandie (CRIANN)', Rouen, France under allocation 1998022, are acknowledged.

References

[1] B. Skews, The perturbed region behind a diffracting shock wave, J. Fluid Mech. 29 (4) (1967) 705.
[2] L. Howard, D. Matthews, On the vortices produced in shock diffraction, J. Appl. Phys. 27 (3) (1956).
[3] T.V. Bazhenova, L.G. Gvosdeva, Y.V. Zhilin, Change in the shape of the diffracting shock wave at a convex corner, Acta Astronaut. 6 (1951) (1979) 401–412.
[4] F. Gnani, K.H. Lo, H. Zare-Behtash, K. Kontis, Experimental investigation on shock wave diffraction over sharp and curved splitters, Acta Astronaut. 99 (1) (2014) 143–152.
[5] M. Sun, K. Takayama, Vorticity production in shock diffraction, J. Fluid Mech. 478 (2003) 237–256.
[6] T. Tseng, R. Yang, Numerical simulation of vorticity production in shock diffraction, AIAA J. 44 (5) (2006) 1040–1047.
[7] A. Chaudhuri, G.B. Jacobs, Dynamics of shock wave diffraction over sharp splitter geometry using entropy-based artificial viscosity method, Shock Waves (2017) 1–15.
[8] M. Sun, K. Takayama, The formation of a secondary shock wave behind a shock wave diffracting at a convex corner, Shock Waves 7 (5) (1997) 287–295.
[9] M.K. Quinn, K. Kontis, A Combined Study on Shock Diffraction, 5th Symposium on Integrating CFD and Experiments in Aerodynamics, 2012, pp. 3–5.
[10] J. Cai, J. Zhou, S. Liu, Z. Lin, Effects of dynamic backpressure on shock train motions in straight isolator, Acta Astronaut. 141 (2017) 237–247.
[11] J. Reeves, B. Skews, Unsteady three-dimensional compressible vortex flows generated during shock wave diffraction, Shock Waves 22 (2) (2012) 161–172.
[12] G. Abate, W. Shyy, Dynamic structure of confined shocks undergoing sudden expansion, Prog. Aero. Sci. 38 (1) (2002) 23–42.
[13] J. Zhao, R. Li, H. Wu, Investigate the shock focusing under a single vortex disturbance using 2D Saint-Venant equations with a shock-capturing scheme, Acta Astronaut. 143 (2018) 337–352.
[14] A. Chaudhuri, A. Hadjadj, O. Sadot, E. Glazer, Computational study of shock-wave interaction with solid obstacles using immersed boundary methods, Int. J. Numer. Methods Eng. 8 (89) (2012) 975–990.
[15] V. Soni, A. Hadjadj, A. Chaudhuri, G. Ben-Dor, Shock-wave reflections over double-concave cylindrical reflectors, J. Fluid Mech. 813 (2017) 70–84.
[16] V. Soni, A. Hadjadj, O. Roussel, On the use of adaptive multiresolution method with time-varying tolerance for compressible fluid flows, Shock Waves (2017) 1–14.
[17] V. Soni, A. Hadjadj, O. Roussel, G. Moebs, Parallel multi-core and multi-processor methods on point-value multiresolution algorithms for hyperbolic conservation laws, J. Parallel Distr. Comput. 123 (2019) 192–203.
[18] A. Chaudhuri, A. Hadjadj, A. Chinnayya, On the use of immersed boundary methods for shock/obstacle interactions, J. Comput. Phys. 230 (5) (2011) 1731–1748.
[19] A. Chaudhuri, A. Hadjadj, A. Chinnayya, S. Palerm, Numerical study of compressible mixing layers using high-order WENO schemes, J. Sci. Comput. 47 (2) (2011) 170–197.
[20] N. Brahmi, A. Hadjadj, V. Soni, A. Chaudhuri, Analysis of shock-wave diffraction over double concave cylindrical wedges, Part I: Shock Dynamics, Acta Astronautica (2020), https://doi.org/10.1016/j.actaastro.2020.01.025.
[21] N.N. Smirnov, V.B. Betelin, V.F. Nikitin, L.I. Stamov, D.I. Altoukhov, Accumulation of errors in numerical simulations of chemically reacting gas dynamics, Acta Astronaut. 117 (2015) 338–355.